processes

MDPI

Article

High-Cycle Fatigue Behavior of Bimetallic Bearing Shell Plates

Renhao Mo [1], Ruoxuan Huang [2,*], Weiping Wang [2], Yang Zhao [2] and Fengming Du [1,*]

[1] Marine Engineering College, Dalian Maritime University, Dalian 116026, China; 19818009254@163.com
[2] College of Transportation Engineering, Dalian Maritime University, Dalian 116026, China; wwp@dlmu.edu.cn (W.W.); 15844525710@163.com (Y.Z.)
* Correspondence: rxhuang@dlmu.edu.cn (R.H.); dfm@dlmu.edu.cn (F.D.)

Abstract

Sliding bearing shells experience repeated bending loads, and fatigue cracking of the copper-alloy working layer can limit their service life. This study evaluated the high-cycle fatigue behavior of steel-backed copper-alloy plates using reciprocating bending tests and finite element fatigue analysis. Specimens were tested at displacement amplitudes of 1.25, 1.50, 2.00, and 2.50 mm under fully reversed loading, with a run-out limit of 10 million cycles. No macroscopic cracks were observed at amplitudes of 1.25–2.00 mm after 10 million cycles; at 2.50 mm, a visible crack appeared at approximately 8.2 million cycles. As displacement amplitude increased from 1.25 to 2.50 mm, the simulated maximum stress rose from 322.31 to 644.62 MPa, while the minimum fatigue safety factor fell from 3.1676 to 0.79191. At 2.50 mm, the predicted high-stress and low-safety-factor regions corresponded spatially to the experimentally observed cracking region. Fracture-surface observations indicated that cracking began at the copper-alloy surface, advanced toward the copper–steel interface, and was followed by cracking in the steel backing near the interface. These findings identify a critical displacement-amplitude range of 2.00–2.50 mm for the tested configuration and show how combined fatigue testing and simulation can help locate fatigue-critical regions in bimetallic bearing plates.

Keywords: bearing shell; bimetallic material; steel-backed copper alloy; reciprocating bending; high-cycle fatigue; failure mechanism

1. Introduction

Sliding bearing shells are key supporting components in the transmission systems of internal combustion engines, reducers, and engineering machinery. During service, cyclic loads, friction, variations in lubrication conditions, and temperature rise can lead to fatigue cracking and local spalling of the working layer. Engineering bearing shells usually use a bimetallic composite structure consisting of a steel backing and a bearing alloy layer. The steel backing provides stiffness and support, while the copper-alloy working layer provides friction-reducing, wear-resistant, and anti-seizure properties. Wear and fatigue are common failure modes of bearing components, and fatigue damage caused by cyclic loading directly affects the service life of bearing shells. Differences in the mechanical properties of steel and copper alloy lead to nonuniform cyclic stress and strain distributions in the bimetallic structure. These differences, together with the interfacial bonding condition, affect local load transfer and make cracking of the working layer, damage to the steel backing, and interfacial separation distinct failure modes that need to be distinguished [1–6].

Previous work has examined bearing fatigue through component failure analysis, material testing, and numerical prediction [7–10]. Quantitative fatigue studies have reported

Check for updates

Academic Editor: Jiaqiang E

Received: 24 September 2026
Revised: 19 October 2026
Accepted: 21 October 2026
Published: 22 October 2026

Copyright: © 2026 by the authors. Licensee MDPI, Basel, Switzerland. This article is an open access article distributed under the terms and conditions of the Creative Commons Attribution (CC BY) license.

measurable effects of manufacturing route and applied pressure. Wang et al. [11] tested SnSb11Cu6 Babbitt–steel bimetallic bearing material and reported a fatigue strength above 40 MPa for material produced by metal inert gas brazing, compared with approximately 35 MPa for material produced by optimized centrifugal casting. This represents a difference of at least about 5 MPa, or roughly 14% relative to the latter value. They also observed that fatigue damage typically initiated as surface microcracks that propagated into the lining and ultimately caused spalling. Dong et al. [12] combined alloy stress–life testing, fluid–structure interaction analysis, and bearing-shell fatigue tests at test loading levels of 20, 27, 34, and 41 MPa. Their results showed that fatigue life decreased rapidly as pressure increased and that numerical predictions agreed well with experimental results. These findings demonstrate that fatigue performance depends on manufacturing route and loading level, and that quantitative assessment requires material-specific experimental data and validated prediction methods.

Interfacial and microstructural studies also provide quantitative evidence of the role of composition and processing. Sun et al. [13] examined Cu–12Sn–xBi–2Ni–1Fe/steel laminated composites with Bi contents of 2 and 6 wt% and bonding times of 1–5 min. Increasing the bonding time promoted growth of the Cu/Fe diffusion layer, while the coefficient of friction decreased with increasing Bi content and bonding time. Liu et al. [14] reported that protective-atmosphere casting of bronze/steel composites limited Pb volatilization to 0.4 wt%; the bronze region had a hardness above 100 HV, and the composite reached maximum tensile and shear strengths of 204.0 and 211.0 MPa, respectively. Xia et al. [15] developed a fatigue-life prediction approach combining continuum damage mechanics, finite-element analysis, and transfer learning for bronze/steel diffusion-welded material; all predicted fatigue-life values fell within a factor-of-two error band around the median experimental lives. At the broader materials level, Bathias and Paris [16] emphasized that fatigue-crack initiation in high- and very-high-cycle regimes depends on local stress concentrations as well as internal defects and microstructural heterogeneity. Peng et al. [17] investigating Cu–xAl/1010 steel composites with Al contents of 0, 6, 7.5, and 9 wt%, reported a metallurgically bonded interface, and found that wear resistance increased with Al content. Wang et al. [18] prepared Cu–Ni–Si/1010 steel laminates by continuous solid/liquid bonding and reported an ultimate tensile strength of 378 MPa, a yield strength of 233 MPa, and an elongation of 25.4%, with no interfacial cracks observed during deformation. In a subsequent study, Wang et al. [19] found that annealing at 450 °C provided the best overall balance of mechanical properties and interfacial bonding, whereas interfacial debonding appeared at annealing temperatures above 500 °C. Peng et al. [20] reported that annealing C61800/1010 steel at 800 °C for 4 h produced a diffusion layer approximately 22.6 μm wide and a γ-free zone approximately 32.1 μm wide, while the bonding strength remained approximately 330–370 MPa. Kang et al. [21] investigated a Cu-20Pb-5Sn/45 steel bimetallic composite and measured an interfacial shear strength of 227.58 MPa, an average friction coefficient of 0.145, and a wear rate of 7.3665×10^{-6} $mm^3/(N \cdot m)$. Together, these studies clarify the roles of interface formation, thermal processing, and composition in the mechanical and tribological performance of copper-alloy/steel composites. However, tensile/shear strength and sliding-wear measurements do not directly establish high-cycle fatigue resistance under displacement-controlled cyclic bending.

Despite these advances, the material-level cyclic fatigue response of steel-backed copper-alloy bimetallic plates under a prescribed displacement ratio remains insufficiently characterized. Recent studies have mainly addressed interface formation, static tensile or shear properties, sliding wear, or full-scale bearing-shell loading, rather than the fatigue-crack initiation and propagation of the bearing plate itself under controlled cyclic bending. In particular, when the number of loading cycles approaches 10^7, the competing damage

behavior of the copper-alloy layer, steel backing, and composite interface under different stress levels has not been sufficiently characterized experimentally. Further investigation is needed to establish whether cracks initiate preferentially in the surface copper-alloy layer, at the composite interface, or in the steel backing, and to determine whether predicted stress-concentration regions correspond to observed crack locations. In this study, bending fatigue tests were conducted on steel-backed copper-alloy bimetallic plates under fully reversed reciprocating displacement loading at displacement amplitudes of 1.25, 1.50, 2.00, and 2.50 mm, with 10^7 cycles used as the run-out criterion. Finite-element stress–life analysis was combined with scanning electron microscopy fractography to compare damage across the loading conditions and assess the relationship between local stress distributions and fatigue cracking.

2. Materials and Methods

2.1. Materials and Specimen Preparation

The material tested was a steel-backed copper-alloy bimetallic plate used for sliding bearing shells. It consisted of a steel backing and a copper-alloy working layer. Before testing, the as-received plate was inspected, and no visible defects, such as macroscopic cracks or delamination, were observed. The plate-shaped fatigue specimen consisted of a clamping section, an arc transition section, and a constant-width working section, as shown in Figure 1. The specimen had an overall length of 160 mm, a width of 20 mm at the wide end and 15 mm at the narrow end, a transition arc radius of 35 mm, and a total thickness of 5.6 mm, comprising a 5.0 mm thick steel backing and a 0.6 mm thick copper-alloy layer.

The fatigue test setup is shown in Figure 2. One end of the specimen was clamped in a fixture, and the other end was connected to the loading actuator. A reciprocating displacement was applied at the free end under fully reversed loading. The adopted cantilever configuration was designed to provide a controlled and reproducible cyclic bending condition for characterizing the high-cycle fatigue response of the bimetallic plate; it was not intended to reproduce the complete multiaxial contact-loading state of an operating sliding bearing shell.

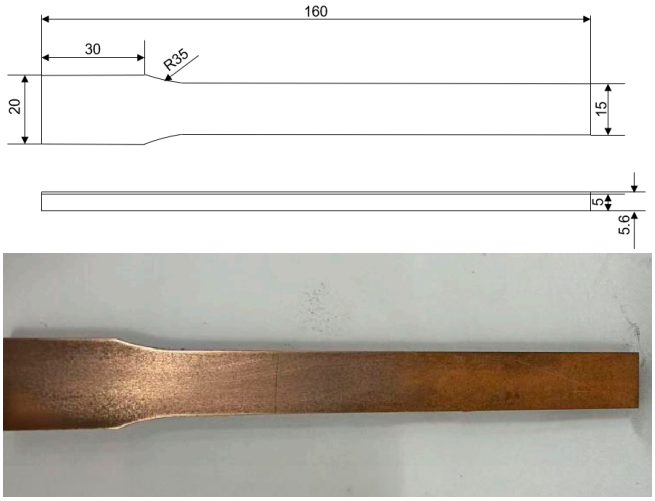


Figure 1. Schematic diagram and sample of bimetallic bearing shell plate.

2.2. Fatigue Test Scheme

The tests were conducted using a reciprocating bending fatigue testing machine. One end of the specimen was clamped, and a reciprocating displacement was applied at the other end. With the initial position taken as the zero point, the displacement amplitudes in the positive and negative directions were equal, with a displacement ratio R = −1. The

displacement amplitudes at the loading end were 1.25, 1.50, 2.00, and 2.50 mm, while all other test conditions were kept constant. Three specimens were tested at each displacement amplitude. A strain gauge was attached at the midpoint of the arc transition section, and strain data were recorded using a strain indicator.

The cutoff number of cycles was set to 10^7 for all displacement amplitudes to investigate the high-cycle fatigue response of the bimetallic plate. If visible fatigue cracks, local fracture, or other identifiable signs of fatigue failure occurred before reaching the cutoff number of cycles, the test was terminated immediately, and the corresponding number of cycles was recorded. If no visible fatigue damage was observed after 10^7 cycles, the test was terminated, and the specimen was considered a run-out at that displacement amplitude.

Because displacement amplitude does not directly correspond to local stress, a finite element (FE) model was established based on the specimen geometry, layered structure, and clamping conditions. The four displacement amplitudes were applied to calculate the stress distribution and identify potential fatigue-critical regions.

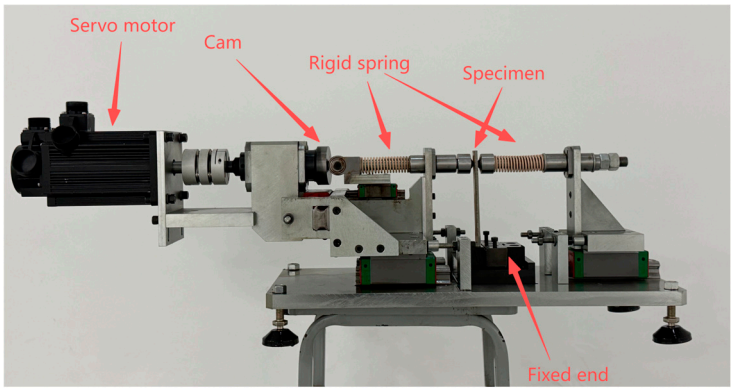


Figure 2. Reciprocating fatigue test setup for bimetallic plates.

3. Finite Element Model and Fatigue Analysis Method

A finite element model of the steel-backed copper-alloy bimetallic specimen was established based on the specimen geometry and clamping configuration, as shown in Figure 3.

3.1. Basic Assumptions of the Model

For the steel-backed copper-alloy bimetallic plate, the following assumptions were adopted in the finite element analysis:

(1) Material homogeneity and continuity.

Both the steel backing and the copper-alloy layer were assumed to be homogeneous, continuous, and isotropic. The influence of microstructural inhomogeneity on the macroscopic stress distribution was neglected.

(2) Perfect interfacial bonding.

A bonded contact condition was applied between the steel backing and the copper-alloy layer to represent the nominal macroscopic load-transfer condition of the bimetallic plate. This assumption does not imply that the real interface is microscopically defect-free. Interfacial slip, debonding, and delamination were not explicitly modeled, and no separate imperfect-interface sensitivity analysis was performed in the present study. The interface model is therefore intended to provide a baseline stress field for identifying fatigue-critical regions rather than to quantitatively predict interfacial fracture.

(3) Geometric idealization.

The finite element model retained the main structural dimensions of the specimen and the arc transition section, while the effects of local factors such as surface roughness,

machining scratches, microscopic defects, and detailed interfacial microstructural heterogeneity were neglected. These idealizations should be considered when interpreting the local stress and fatigue-safety-factor predictions.

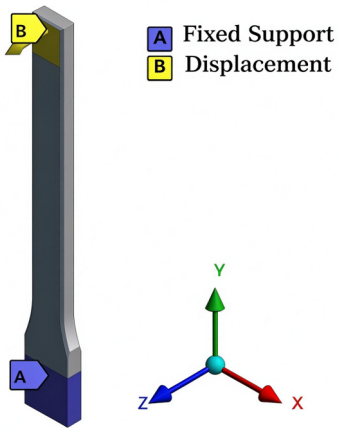


Figure 3. Schematic diagram of the finite element model.

3.2. Governing Equations for Fatigue Analysis

The stress–life method (S–N method) was used to evaluate the high-cycle fatigue behavior [22–24]. The quasi-static stress field at each displacement amplitude was first calculated, and the equivalent alternating stress amplitude was then determined from the fully reversed cyclic loading condition. Separate S–N relationships were used for the copper-alloy layer and the steel backing. The S–N curves were fitted using an exponential quadratic polynomial function of ln N, and the corresponding fitted relationships are given in Equations (5) and (6). Thus, the allowable alternating stress at the target life was obtained from the material-specific S–N relationship rather than from a single curve for the entire bimetallic plate.

For the fatigue-strength input, the steel-backing and copper-alloy S–N curves were fitted separately from the available S–N data using the exponential quadratic polynomial representation in ln N. The fitted functions are provided in Equations (5) and (6), respectively, and were used to obtain the allowable alternating stress at N = 10^7 cycles.

(1) Governing Equations for Static Equilibrium

Assuming that inertia effects are negligible and the loading process is quasi-static, the bimetallic plate satisfies the static equilibrium equation:

$$\nabla \cdot \sigma + b = 0 \tag{1}$$

where σ is the stress tensor and b is the body force per unit volume. In this study, loading was applied as a prescribed displacement. Since the self-weight effect is negligible compared with the cyclic bending load, the body force was neglected:

$$b = 0 \tag{2}$$

For a small-strain linear elastic problem, the strain–displacement relationship is:

$$\varepsilon = \frac{1}{2}\left[\nabla u + (\nabla u)^{\mathrm{T}}\right] \tag{3}$$

where ε is the strain tensor and u is the displacement vector.

Both the steel backing and the copper-alloy layer were modeled as isotropic linear elastic materials:

$$\sigma = D\varepsilon \tag{4}$$

where D is the elasticity matrix, which depends only on the elastic modulus E and Poisson's ratio ν.

By solving the above equations, the stress fields at the four displacement amplitudes were obtained and used as input for the subsequent fatigue analysis.

(2) S–N curve functions

The S–N curves of the copper-alloy layer and the steel backing were fitted using an exponential quadratic polynomial function in terms of $\ln N$. The fatigue strength $S(N)$ of the steel backing was expressed as:

$$S(N) = \exp\left(0.162(\ln N)^2 - 2.52\ln N + 9.49\right) \tag{5}$$

The fatigue strength $S(N)$ of the copper-alloy layer was expressed as:

$$S(N) = \exp\left(-0.0394 \cdot (\ln N)^2 + 0.0205 \cdot \ln N + 5.93\right) \tag{6}$$

(3) Fatigue safety factor

To evaluate the fatigue safety margin of the bimetallic plate at different displacement amplitudes, the fatigue safety factor was defined as:

$$F_s = \frac{\sigma_{a,N}}{\sigma_{a,\mathrm{eq}}} \tag{7}$$

where $\sigma_{\mathrm{a,eq}}$ is the local equivalent alternating stress amplitude obtained from the finite element analysis. The S–N relationships in Equations (5) and (6) were fitted separately for the steel backing and copper-alloy layer. The present S–N formulation does not introduce a separate probabilistic reliability correction; therefore, the reported safety factors are not assigned to a specific survival probability such as 50% or 97.7%.

The target fatigue life was set to:

$$N = 1 \times 10^7 \tag{8}$$

Therefore,

$$F_s = \frac{\sigma_{a,10^7}}{\sigma_{a,\mathrm{eq}}} \tag{9}$$

When

$$F_s > 1 \tag{10}$$

the corresponding location has a fatigue safety margin at the target life of 10^7 cycles. When

$$F_s = 1 \tag{11}$$

the local equivalent stress amplitude equals the fatigue strength at the specified fatigue life. When

$$F_s < 1 \tag{12}$$

the local equivalent stress amplitude exceeds the fatigue strength, indicating a risk of fatigue failure at the target life.

(4) Mean stress treatment

The directly controlled parameter in the experiment was the displacement at the loading end. Since the displacement amplitudes in the positive and negative directions were equal, the displacement ratio was R = −1. Accordingly, the nominal stress cycle was treated as fully reversed, with approximately zero mean stress, so no mean-stress correction was applied in the S–N evaluation.

$$R_\delta = -1 \tag{13}$$

The stress tensors induced by the positive and negative displacements have opposite signs, and for the same stress component, the following approximate relation holds:

$$\sigma_{\min} \approx -\sigma_{\max} \tag{14}$$

3.3. Boundary Conditions and Loading Settings

To ensure consistency between the finite element model and the fatigue test conditions, the boundary conditions were defined based on the actual test configuration, in which one end of the specimen was clamped and a prescribed displacement was applied at the other end, as shown in Figure 3.

(1) Fixed constraint

A fixed constraint was applied to the clamped end of the specimen, constraining all translational degrees of freedom:

$$U_X = U_Y = U_Z = 0 \tag{15}$$

(2) Displacement loading

Displacement amplitudes consistent with those used in the fatigue tests were applied at the loading end:

$$\delta = 1.25,\ 1.50,\ 2.00,\ 2.50 \text{ mm} \tag{16}$$

Fully reversed cyclic loading was applied, with R = −1, and the cutoff number of cycles was set to 10^7. The present loading condition provides a controlled fatigue characterization of the specimen and does not reproduce all service-specific effects of sliding bearing shells, such as contact pressure, friction, lubrication, thermal loading, and complex multiaxial stress states.

4. Results and Discussion

4.1. Stress Distribution Under Different Displacement Amplitudes

Figure 4 shows the stress distributions of the specimens under different displacement amplitudes. As the displacement amplitude increased from 1.25 to 1.50, 2.00, and 2.50 mm, the corresponding maximum stresses were 322.31, 386.77, 515.70, and 644.62 MPa, respectively. The overall stress distribution patterns and the locations of the high-stress regions were essentially consistent under all loading conditions, indicating that, within this displacement range, the displacement amplitude primarily affected the stress level without significantly changing the stress distribution characteristics of the specimen. The high-stress regions were mainly located near the loading end and the arc transition section on the fixed side, where pronounced local stress concentrations occurred. These regions are therefore critical for fatigue damage analysis. Under the same cyclic loading conditions, a larger displacement amplitude led to a higher cyclic stress level, thereby increasing fatigue damage accumulation and the risk of fatigue crack initiation. Because the high-stress region remained spatially consistent, no amplitude-dependent shift of the predicted critical location was identified.

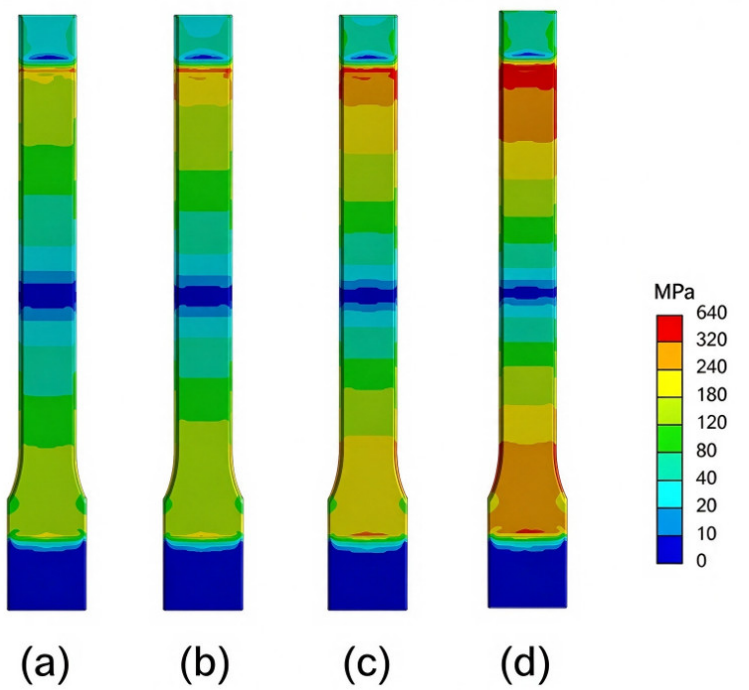


Figure 4. Stress distributions under different displacement amplitudes: (**a**) 1.25 mm; (**b**) 1.5 mm; (**c**) 2.0 mm; (**d**) 2.5 mm.

4.2. Fatigue Safety Factor Distribution Under Different Displacement Amplitudes

Figure 5 shows the fatigue safety factor distributions of the steel-backed copper-alloy bimetallic plate under different displacement amplitudes. As the displacement amplitude increased from 1.25 to 1.50, 2.00, and 2.50 mm, the minimum fatigue safety factors were 3.1676, 1.5838, 1.0559, and 0.79191, respectively, indicating that the fatigue safety margin decreased progressively with increasing displacement amplitude. The regions with low safety factors were mainly located near the loading end and the lower transition region, and these regions expanded gradually as the displacement amplitude increased. These low-safety-factor regions corresponded to areas with relatively high local stress and thus represented potential fatigue-critical locations. At a displacement amplitude of 2.00 mm, the minimum safety factor was already close to unity, indicating a relatively small safety margin under the target fatigue life and the adopted fatigue evaluation criterion. At a displacement amplitude of 2.50 mm, the minimum safety factor fell below 1, indicating that the local region was predicted to be unable to sustain the target 10^7-cycle life under the adopted S–N criterion. This result is interpreted as a life-regime indication rather than a direct prediction of the exact crack-initiation cycle.

4.3. Experimental Fatigue Results and Crack Initiation Analysis

During the fatigue tests, strain data were recorded using a strain measurement system, and the strain data acquisition interface is shown in Figure 6. At displacement amplitudes of 1.25, 1.50, and 2.00 mm, no visible cracking, peeling, or spalling was observed on the surface of the copper-alloy layer after the specimens completed 10^7 cycles. At a displacement amplitude of 2.50 mm, however, the first visible macroscopic crack was recorded at approximately 8.2×10^6 cycles, as shown in Figure 7. This corresponds to approximately 82% of the 10^7-cycle cutoff. These results establish a critical displacement-amplitude range of 2.00–2.50 mm for the present test conditions and 10^7-cycle criterion. Because only discrete displacement amplitudes were tested, the present data do not establish whether the transition is intrinsically abrupt or gradual, nor do they determine an exact fatigue limit between 2.00 and 2.50 mm.

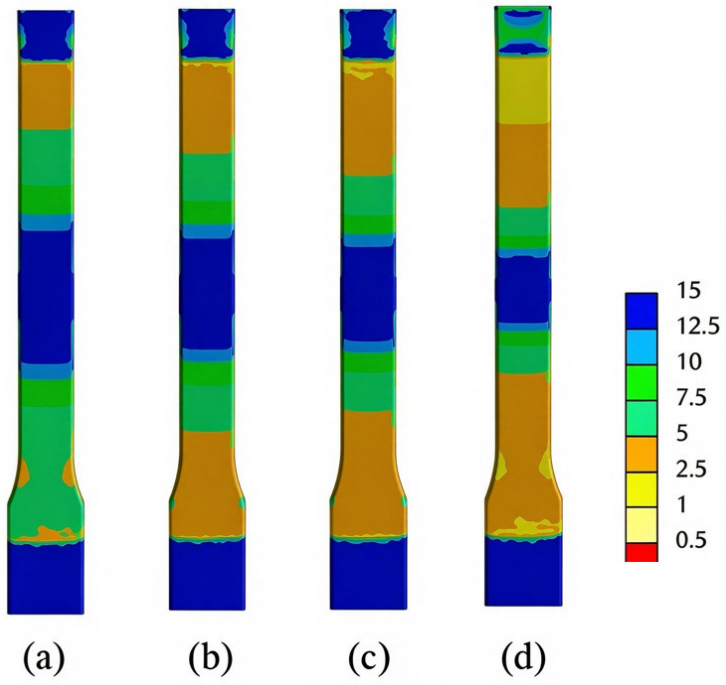


Figure 5. Distributions of fatigue safety factor under different displacement amplitudes: (**a**) 1.25 mm; (**b**) 1.5 mm; (**c**) 2.0 mm; (**d**) 2.5 mm.

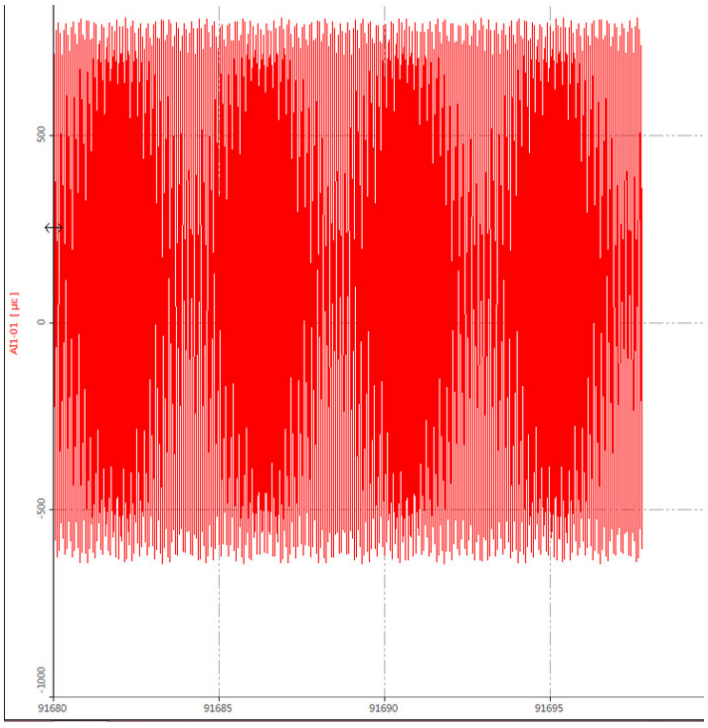


Figure 6. Strain history recording.

The low-safety-factor and high-fatigue-damage regions predicted by the simulation were spatially consistent with the actual fatigue crack initiation region observed in the experiment at 2.50 mm. The agreement supports the use of the FE/S–N framework for identifying the macroscopic critical region under the tested loading condition. However, because continuous crack-growth measurements and crack-front coordinates were not obtained, the present study does not claim quantitative prediction of crack-growth rate or exact crack-initiation position. The experimental crack initiation at approximately

8.2×10^6 cycles, together with the simulated safety factor below unity at 2.50 mm, indicates consistency in the predicted fatigue-life regime.

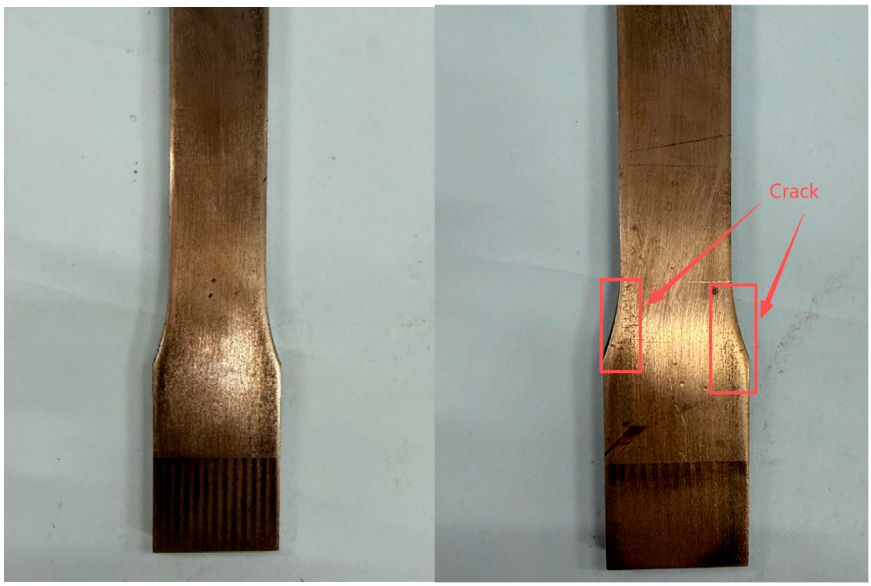


Figure 7. Specimen without cracks (**left**) and specimen with cracks (**right**).

4.4. Fatigue Fracture Morphology and Failure Mechanism

To observe the fatigue fracture morphology, the specimen tested at a displacement amplitude of 2.50 mm was subjected to continued fatigue testing until complete fracture occurred. The fracture morphology is shown in Figure 8, with the lower-right corner further magnified in the inset. On the overall fracture surface, the copper-alloy layer is on the right side, and the steel backing is on the left side. Numerous irregular pores and interparticle gaps were observed in the copper-alloy region, consistent with the powder-sintering process used for this layer. However, some cavities on the fracture surface may also have formed through particle separation or detachment during fracture. Because this region is near the specimen edge, pores and regions of weak interparticle bonding may have acted as local fatigue damage initiation sites. Therefore, the copper-alloy surface at the lower-right corner was identified as the fatigue crack initiation location. The fracture surface of the steel backing on the left was relatively continuous, with fine undulating textures and local ridges. Based on the experimental observations and fracture characteristics, after the copper-alloy layer cracked, the local load-transfer behavior near the interface changed, and fatigue cracking was subsequently observed in the steel backing near the interface. These observations identify the copper/steel interface as an important crack-path transition region, but they are insufficient to determine conclusively whether the interface acts as a crack arrestor or a weak link. No dedicated interfacial debonding test or detailed cross-sectional interface characterization was performed in the present study. The discussion is therefore limited to the observed fracture sequence and the associated change in local load transfer.

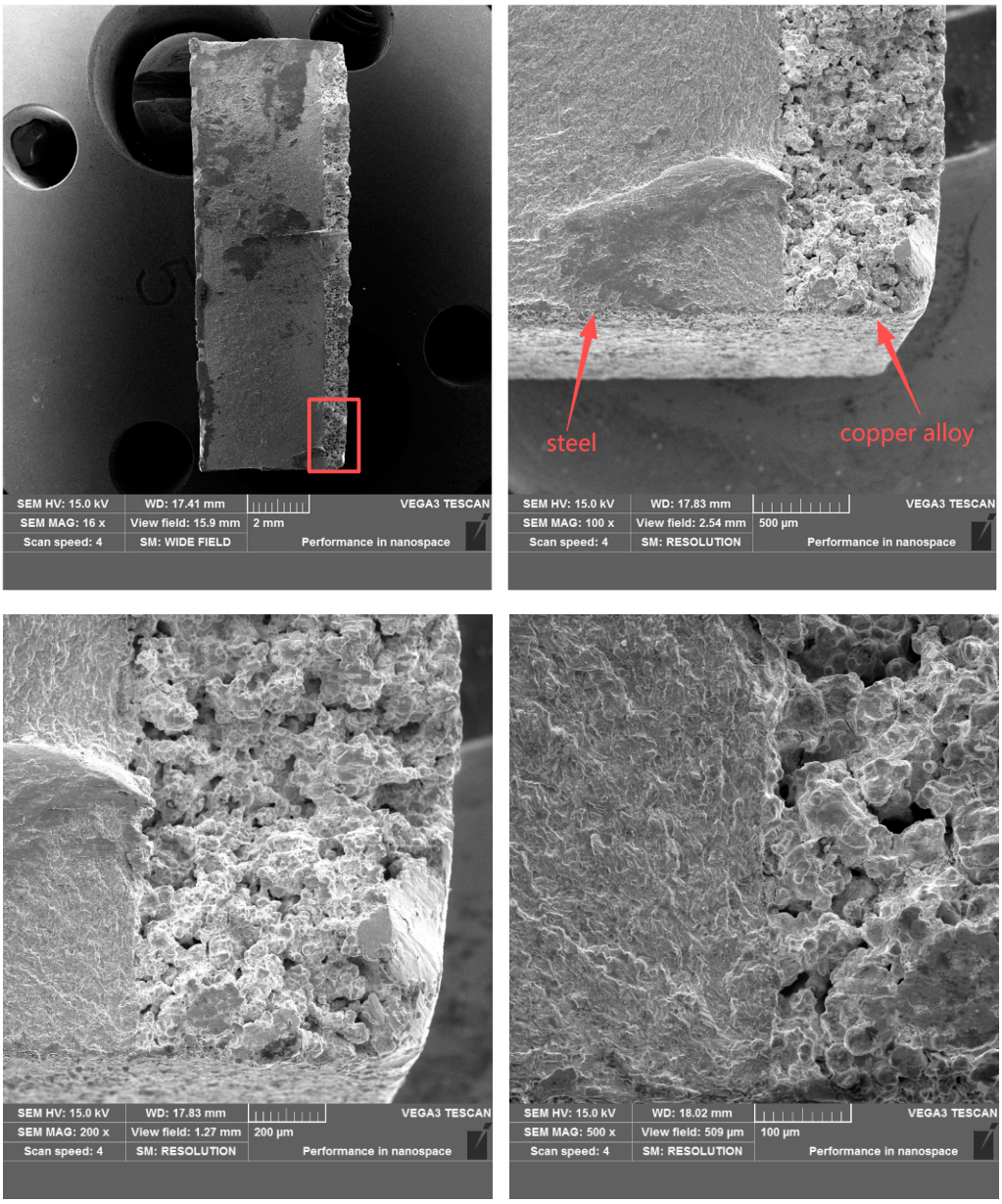


Figure 8. Fracture morphology analysis.

5. Conclusions

In this study, steel-backed copper-alloy bimetallic plates for sliding bearing shells were investigated. High-cycle fatigue tests were conducted under fully reversed reciprocating displacement loading, and finite element analysis combined with SEM observations of fracture surfaces was used to investigate the fatigue performance of the bimetallic plates under different displacement amplitudes. The main conclusions are as follows:

(1) After 10^7 cycles, no macroscopic fatigue cracks were observed in specimens tested at displacement amplitudes of 1.25, 1.50, and 2.00 mm. At a displacement amplitude of 2.50 mm, the first visible macroscopic crack was recorded at approximately 8.2×10^6 cycles. Therefore, under the test conditions used in this study, the critical displacement-amplitude range associated with the 10^7-cycle criterion is 2.00–2.50 mm. Because no intermediate amplitudes were tested, an exact fatigue limit and the abruptness or gradualness of the transition cannot be determined.

(2) Finite element simulation results showed that the maximum stress increased approximately linearly from 322.31 to 644.62 MPa as the displacement amplitude increased

from 1.25 to 2.50 mm. Correspondingly, the minimum fatigue safety factor decreased from 3.1676 to 0.79191, indicating that the local fatigue safety margin decreased with increasing displacement amplitude.

(3) The regions of relatively high stress and low fatigue safety factor in the arc transition section near the fixed end were spatially consistent with the experimentally observed macroscopic cracking location at 2.50 mm. This agreement supports the use of the FE/S–N analysis to identify the macroscopic fatigue-critical region under the controlled bending condition. The present study does not claim quantitative crack-growth prediction because continuous crack-growth data were not obtained.

(4) Fractographic observations showed that fatigue cracks initiated at the surface of the copper-alloy layer and then propagated toward the copper–steel interface. Cracking on the steel side was subsequently observed near the interface and propagated into the steel.

Author Contributions: Writing—original draft, R.M.; data curation, W.W., Y.Z. and R.H.; writing—review and editing, F.D. All authors have read and agreed to the published version of the manuscript.

Funding: This research was supported by Fundamental Research Funds for the Central Universities (3132026512).

Data Availability Statement: The data presented in this study are available from the corresponding authors upon reasonable request.

Conflicts of Interest: The authors declare no conflicts of interest.

References

1. Xu, F.N.; Ding, N.; Li, N.; Liu, L.; Hou, N.; Xu, N.; Guo, W.M.; Tian, L.N.; Xu, H.X.; Wu, C.-M.L.; et al. A review of bearing failure modes, mechanisms and causes. *Eng. Fail. Anal.* **2023**, *152*, 107518. [CrossRef]
2. Sous, C.; Wünsch, H.; Jacobs, G.; Broeckmann, C. Prediction of fatigue limit of journal bearings considering a multi-axial stress state. *Ind. Lubr. Tribol.* **2016**, *68*, 430–438. [CrossRef]
3. El-Daher, C.C.; Kebir, H.; Bouvier, S.; Pont, M.; Hay, M. Prediction of fatigue damage and spalling in a multilayered journal bearing shell. *Tribol. Int.* **2022**, *175*, 107850. [CrossRef]
4. Guo, Y.; Wu, X.; Ren, G.; Liu, Z.; Yuan, R.; Yang, X.; Dong, P. Microstructure and properties of copper-steel bimetallic plates prepared by friction stir additive manufacturing. *J. Manuf. Process.* **2022**, *82*, 689–699. [CrossRef]
5. Zhang, H.; Jiao, K.X.; Zhang, J.L.; Liu, J. Experimental and numerical investigations of interface characteristics of copper/steel composite prepared by explosive welding. *Mater. Des.* **2018**, *154*, 140–152. [CrossRef]
6. Liu, Y.; Li, B.; Zhang, W.; Liu, Z.; Jiang, M. Interfacial behavior of copper/steel bimetallic composites fabricated by CMT-WAMM. *Coatings* **2024**, *14*, 803. [CrossRef]
7. Blundell, J.K. Fatigue initiation in thin-wall journal bearings. *ASLE Trans.* **1980**, *23*, 131–140. [CrossRef]
8. McCallion, H.; Lotfi, M. Tensile surface stresses and fatigue in plain journal bearings. *Tribol. Int.* **1992**, *25*, 247–257. [CrossRef]
9. Wang, Q.; Zheng, Q.F.; Li, D.F. LIDF Development of Copper Alloy-Steel Bimetallic Bearing Materials and Manufacturing Technology. *Mater. Sci. Forum* **2020**, *993*, 374–383. [CrossRef]
10. Sudhakar, V.; Cruz Paredes, J. Failure mechanisms in motor bearings. *Eng. Fail. Anal.* **2005**, *12*, 35–42. [CrossRef]
11. Wang, X.B.; Yin, Z.W.; Chen, Y.H. Study on fatigue strength of SnSb11Cu6 babbitt-steel bimetal sliding bearing material prepared by MIG brazing. *Mech. Ind.* **2020**, *21*, 106. [CrossRef]
12. Dong, Q.; Yin, Z.W.; Li, H.L.; Gao, G.Y.; Zhong, N.; Chen, Y.H. Simulation and experimental verification of fatigue strength evaluation of journal bearing bush. *Eng. Fail. Anal.* **2020**, *109*, 104275. [CrossRef]
13. Sun, J.; Wang, M.; Peng, B.; Zhao, Z.; Dong, B.; Yi, H.; Li, T.; Jie, J. Tailoring microstructure and performance of Cu/steel bimetallic laminated composites by Bi content and bonding time regulation. *J. Mater. Res.* **2026**, *41*, 1891–1902. [CrossRef]
14. Liu, B.; Sui, D.-S.; Guo, Z.-M.; Wang, Y.-L.; Yang, X.-L.; Hu, G.-H.; Zhang, J.-X.; Luo, C.-Z. Microstructural characteristics and mechanical properties of bronze/steel bimetallic laminated composite prepared by protective atmosphere casting process. *China Foundry* **2021**, *18*, 497–504. [CrossRef]
15. Xia, Q.; Ji, C.; Zhan, Z.; Wang, X.; Bian, Z.; Hu, W.; Meng, Q. Damage mechanics coupled with a transfer learning approach for the fatigue life prediction of bronze/steel diffusion welded bimetallic material. *Int. J. Fatigue* **2025**, *188*, 108631. [CrossRef]
16. Bathias, C.; Paris, P.C. *Gigacycle Fatigue in Mechanical Practice*; Marcel Dekker: New York, NY, USA, 2005. [CrossRef]

17. Peng, B.; Hang, Z.; Jie, J.; Lou, S.; Wang, H.; Muraishi, S.; Li, T. Evolution of interface and mechanical performance of Cu-xAl/1010 steel bimetal laminated composite. *J. Alloys Compd.* **2023**, *935*, 168121. [CrossRef]
18. Wang, M.; Sun, J.; Peng, B.; Dong, B.; Jie, J.C.; Li, T.J. Interfacial bonding mechanism and mechanical properties of Cu-Ni-Si/1010 steel bimetallic laminated composites prepared by continuous solid/liquid bonding. *Mater. Today Commun.* **2024**, *40*, 109803. [CrossRef]
19. Wang, M.; Peng, B.; Sun, J.; Wang, X.; Li, G.; Wang, X.; Jie, J.; Li, T. Simultaneously enhancing mechanical and bonding property of Cu-Ni-Si/1010 steel bimetal laminated composites via annealing. *Mater. Charact.* **2025**, *223*, 114908. [CrossRef]
20. Peng, B.; Li, G.; Hang, Z.; Liu, J.; Shan, X.; Jie, J.C.; Li, T.J. Effect of annealing on the microstructure evolution and interfacial diffusion layer of C61800/1010 steel bimetal laminated composites. *Mater. Today Commun.* **2025**, *44*, 112133. [CrossRef]
21. Kang, Y.; Zhang, G.; Hu, Y.; Liu, Y. Interfacial diffusion and copper alloy layer wear mechanism in Cu-20Pb-5Sn/45 steel bimetallic composites. *Coatings* **2025**, *15*, 1072. [CrossRef]
22. Joyce, M.R.; Reed, P.A.S.; Syngellakis, S. Numerical modelling of crack shielding and deflection in a multi-layered material system. *Mater. Sci. Eng. A* **2003**, *342*, 11–22. [CrossRef]
23. Mwanza, M.C.; Joyce, M.R.; Lee, K.K.; Syngellakis, S.; Reed, P.A.S. Microstructural characterisation of fatigue crack initiation in Al-based plain bearing alloys. *Int. J. Fatigue* **2003**, *25*, 1135–1145. [CrossRef]
24. Matsuba, A.; Torii, T. Fatigue crack propagation behavior in laminated composite materials using pure copper and carbon steel (Composite 1). *Proc. Asian Pac. Conf. Fract. Strength Int. Conf. Adv. Technol. Exp. Mech.* **2001**, *2.01.03*, 557–562. [CrossRef]

Disclaimer/Publisher's Note: The statements, opinions and data contained in all publications are solely those of the individual author(s) and contributor(s) and not of MDPI and/or the editor(s). MDPI and/or the editor(s) disclaim responsibility for any injury to people or property resulting from any ideas, methods, instructions or products referred to in the content.